11-2021

Identification of an Intermediate Species along the Nitrile Hydratase Reaction Pathway by EPR Spectroscopy

Wasantha Lankathilaka Karunagala Pathiranage
Marquette University

Natalie Gumataotao
Loyola University Chicago

Adam T. Fiedler
Marquette University, adam.fiedler@marquette.edu

Richard C. Holz
Marquette University, richard.holz@marquette.edu

Brian Bennett
Marquette University, brian.bennett@marquette.edu

Biochemistry, Vol. 60, No. 49 (November 2021): 3771-3782. DOI.

Identification of an Intermediate Species along the Nitrile Hydratase Reaction Pathway by EPR Spectroscopy

Wasantha Lankathilaka Karunagala Pathiranage
Department of Chemistry, Marquette University, Milwaukee, Wisconsin
Natalie Gumataotao
Department of Chemistry and Biochemistry, Loyola University, Chicago, Illinois
Adam T. Fiedler
Department of Chemistry, Marquette University, Milwaukee, Wisconsin
Richard C. Holz
Department of Chemistry, Marquette University, Milwaukee, Wisconsin
Brian Bennett
Department of Physics, Marquette University, Milwaukee, Wisconsin

Abstract

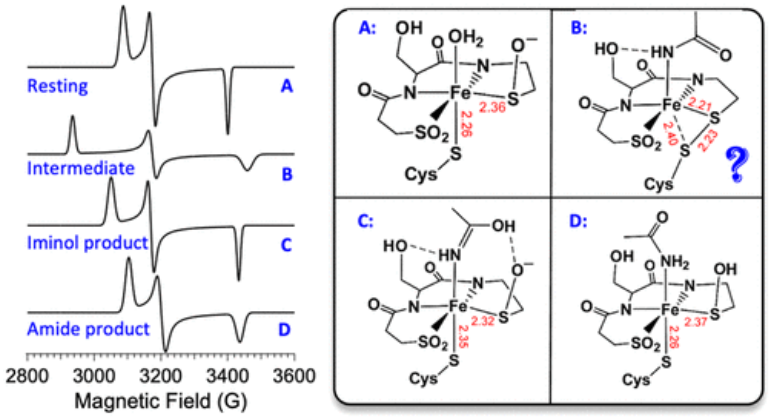

A new method to trap catalytic intermediate species was employed with Fe-type nitrile hydratase from *Rhodococcus equi* TG328-2 (*Re*NHase). *Re*NHase was incubated with substrates in a 23% (w/w) NaCl/H_2O eutectic system that remained liquid at −20 °C, thereby permitting the observation of transient species that were present at electron paramagnetic resonance (EPR)-detectable levels in samples frozen while in the steady state. Fe^{III}-EPR signals from the resting enzyme were unaffected by the presence of 23% NaCl, and the catalytic activity was ∼55% that in the absence of NaCl at the optimum pH of 7.5. The reaction of *Re*NHase in the eutectic system at −20 °C with the substrates acetonitrile or benzonitrile induced significant changes in the EPR spectra. A previously unobserved signal with highly rhombic *g*-values (g_1 = 2.31) was observed during the steady state but did not persist beyond the exhaustion of the substrate, indicating that it arises from a catalytically competent intermediate. Distinct signals due to product complexes provide a detailed mechanism for product release, the rate-limiting step of the reaction. Assignment of the observed EPR signals was facilitated by density functional theory calculations, which provided candidate structures and *g*-values for various proposed *Re*NHase intermediates. Collectively, these results provide new insights into the catalytic mechanism of NHase and offer a new approach for isolating and characterizing EPR-active intermediates in metalloenzymes.

Introduction

Nitrile hydratases (NHases, EC 4.2.1.84) are metalloenzymes that contain either low-spin (*S* = 1/2) Fe(III) (Fe-type) or low-spin (*S* = 0) Co(III) (Co-type) ions in their active site. (1,2) X-ray crystallographic studies on NHases revealed that they are $\alpha_2\beta_2$ heterotetramers with an active site metal ion coordinated by three cysteine (Cys) residues and two amidate nitrogens derived from the protein backbone yielding a coordination geometry referred to as a “claw-setting”. (3,4) Two of the active site cysteine residues are post-translationally modified to cysteine–sulfinic acid (−SO_2H) and cysteine–sulfenic acid (−SOH), respectively, while the axial cysteinate ligand remains unaltered. The protonation states of the active site equatorial sulfenic and sulfinic acid iron-ligands have been proposed to be neutral Cys–SOH and anionic Cys–SO_2^-, based on sulfur K-edge X-ray absorption spectroscopy (XAS) and geometry-optimized density functional theory (DFT) calculations. (5) Oxidation of the equatorial Cys residues is essential for catalysis and the catalytic relevance of these moieties is well-established, (6) but information concerning their mechanistic roles and the catalytic significance of their protonation states is only just starting to evolve. (7)

Biomimetic NHase models and structure/function studies on NHase enzymes have yielded insights into the catalytic mechanism. However, models that display activity are scarce, and the rational design is hampered by insufficient understanding of the mechanism of NHase itself. (8−12) From X-ray crystallography, stopped-flow kinetics, and electron paramagnetic resonance (EPR) spectroscopic evidence, (13−15) a catalytic mechanism was

proposed with a heretofore unknown role for the sulfenic acid (αCys–OH) ligand as an active site nucleophile (Figure 1). (15) This unique chemistry was subsequently corroborated by time-resolved X-ray crystallography and DFT calculations. (7,16−18) Salient features of this mechanism include (i) direct coordination of the nitrile substrate to the active site metal center (13,17) and (ii) activation of the bound nitrile bond toward nucleophilic attack by the αCys–OH ligand, forming a cyclic intermediate (**I** in Figure 1). Subsequent $^{16/18}O$ mass spectrometric studies (19) found that the product amide oxygen is protein-, rather than water-derived, providing further support for active participation by the sulfenic acid (αCys–OH) ligand. Once the cyclic intermediate is formed, it must react with H_2O to generate the amide product, and two possible pathways have been proposed for this portion of the catalytic mechanism (Figure 1). In the first route (**A**), a water-derived nucleophile attacks the S-atom of the cyclized unit, cleaving the S–O bond and regenerating the sulfenic acid ligand. An alternative route (**B**) is based on recent theoretical studies that suggest that S–O bond cleavage is accompanied by the formation of a disulfide bond with the axial Cys ligand (**II** in Figure 1). (16,18,20) In this scenario, the sulfenic acid ligand is then regenerated by the reaction of the disulfide moiety with H_2O. In both pathways, once nucleophilic attack of the nitrile carbon occurs, two water-derived protons are transferred in the rate-limiting step. (21,22) As shown in Figure 1, the nascent product may exist as an iminol ligand (**III**) that subsequently tautomerizes to an amide. The amide product is then displaced by a water molecule in the final step, thereby regenerating the catalyst.

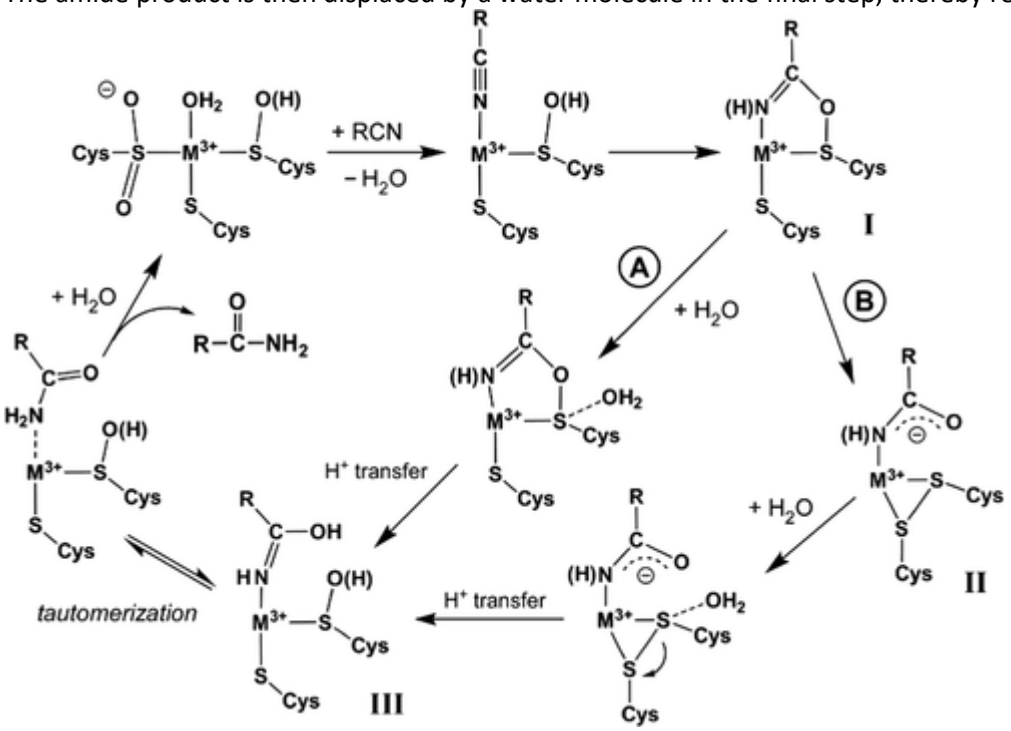

Figure 1. Proposed catalytic cycle for NHase. The cysteine–sulfinic acid moiety shown in the resting enzyme is omitted in subsequent structures for compactness.

Elucidation of the NHase reaction pathway requires the trapping of catalytic intermediates amenable to spectroscopic characterization, as well as computational methods capable of translating the spectroscopic data into structural information. To identify intermediate species and provide insight into the catalytic mechanism of NHases, we report herein a novel cryoenzymological approach that utilizes a 23% (w/w) $NaCl/H_2O$ eutectic system that can be cooled to −20 °C while remaining in the liquid state. This approach was developed after attempts to employ rapid-freeze-quench (RFQ) techniques were unsuccessful due to the incompatibility of Fe-type NHase with various solvents. In contrast, EPR spectra of the Fe-type nitrile hydratase from *Rhodococcus equi* TG328-2 (*Re*NHase) recorded on samples frozen after being cooled to −20 °C in this eutectic system were indistinguishable from resting EPR signals observed in the absence of NaCl. Moreover, the enzyme in the liquid eutectic retained ∼55% of its catalytic activity at the optimum pH of 7.5. The reaction of *Re*NHase and the slow

substrate acetonitrile (ACN) in 23% (w/w) NaCl/H_2O at −20 °C revealed a novel EPR signal in the steady state. This signal arises from a catalytically competent intermediate that has not been observed in prior NHase studies. Insights into the structural identity of this intermediate were gained from density functional theory (DFT) calculations that provided computed *g*-values for proposed active-site structures. This combined spectroscopic and computational approach was also applied to the product-bound enzyme, providing compelling evidence in support of the iminol/amide tautomerization shown in Figure 1. In addition to advancing our understanding of the NHase catalytic cycle, the novel methods and procedures described here can be applied to future mechanistic studies of EPR-active metalloenzymes. In particular, it is shown that the NaCl/H_2O eutectic system offers an alternative to traditional RFQ techniques for the trapping of transient species.

Materials and Methods

Materials

All reagents were purchased commercially and were of the highest purity available. Ampicillin, kanamycin, *N*-2-hydroxyethylpiperazine-*N*-2-ethanesulfonic acid (HEPES), 2-(*N*-morpholino)ethanesulfonic acid (MES), *N*-cyclohexyl-2-aminoethanesulfonic acid (CHES), isopropyl-β-d-1- thiogalactopyranoside (IPTG), acrylonitrile, acetonitrile, benzonitrile, 3-hydroxybenzonitrile, 3,4-dihydroxybenzonitrile, 2-methylbutane (2-MeBu), 2-methylpentane, and pentane were purchased from Sigma-Aldrich or Fisher scientific.

Expression and Isolation of *Re*NHase

NHase was isolated using an anaerobic protocol as previously described in detail. (23) Briefly, the α and β genes were inserted into a pET 28a$^+$ plasmid and the ε gene was inserted into a pET 21a$^+$ plasmid, and the genes were co-expressed in *Escherichia coli* BL21 DE3 cells. The active enzyme was isolated using two anion exchange chromatography steps, eluted with NaCl, with an intervening metal affinity chromatography step, eluted with imidazole.

Steady-State Kinetic Assays

The enzymatic activities at 25 °C of 20–200 nM *Re*NHase in 2.5 mM HEPES buffer, pH 7.5, toward the substrates 1–400 μM benzonitrile (benzamide; $\Delta\varepsilon_{244}$ = 3.49 mM^{-1} cm^{-1}), 1–400 μM 3-hydroxybenzonitrile (3-hydroxybenzamide; $\Delta\varepsilon_{247}$ = 2.19 mM^{-1} cm^{-1}), 1–400 μM 3,4-dihydroxybenzonitrile (3,4-dihydroxybenzamide; $\Delta\varepsilon_{264}$ = 4.04 mM^{-1} cm^{-1}), 1–100 mM acrylonitrile (acrylamide; $\Delta\varepsilon_{225}$ = 2.9 mM^{-1} cm^{-1}), and 1–100 mM acetonitrile (acetamide; $\Delta\varepsilon_{220}$ = 4.96 × 10^{-2} mM^{-1} cm^{-1}) were determined spectrophotometrically. The kinetic constants V_{max} and K_m were calculated by fitting the data to the Michaelis–Menten equation in OriginPro 9.0. Arrhenius equation coefficients E_a and A were estimated from fitting plots of ln(activity) vs 1/T (K) using activities measured between 5 and 35 °C.

Trapping Reaction Intermediates for *Re*NHase

Three approaches for presteady-state EPR spectrokinetics were evaluated. One was the use of traditional rapid-freeze-quench (RFQ), using 2-methylbutane (isopentane) at −95 °C as a nominally inert, immiscible cryogen with a freezing time of 4 ms under the conditions employed. A second approach utilized cryoenzymology, in which *Re*NHase was dissolved in a eutectic system of an aqueous buffer solution and dimethyl sulfoxide (DMSO) that remains liquid at temperatures down to −80 °C. Under certain conditions, such a mixture can be exploited to significantly slow an enzymatic reaction and allow intermediates to be subsequently trapped by manual freezing techniques. (24) Both of these methods ultimately proved unsuitable with NHase (vide infra).

Finally, a third, apparently unreported method was chosen that utilized a eutectic (cryohydratic) system whereby a 23% by weight solution of NaCl in buffer provided a melting temperature $T°_{23\%}$ of −21 °C. Such a salt solution containing 32.5 mM HEPES at pH 7.5 (hereafter referred to as “CSS 7.5”) remained liquid indefinitely in

a commercial −20 °C freezer (measured sample temperature −18 to −20 °C; Fluke 2165A Digital Thermometer). Solutions of resting *Re*NHase in CSS 7.5 were prepared, the catalytic activities were measured, and the EPR spectra of the subsequently frozen samples were recorded. Analogous samples were similarly prepared containing 32.5 mM MES pH 5.0, CHES pH 9.0, CHES pH 9.5, and CHES pH 10.0 (CSS 5.0, CSS 9.0, CSS 9.5, and CSS 10.0, respectively). Separate aliquots of 100 µM *Re*NHase and 250 µM acetonitrile in CSS at each pH were prepared. For studies with benzonitrile, a saturated solution of benzonitrile in buffer was prepared, and then the appropriate amount of NaCl was added to make CSS.

For EPR studies, a 150 µL slug of the substrate solution was placed in the lower half, leaving an air gap of about 3 cm to the bottom of a 3 mm I.D. EPR tube (707-SQ-250M, Wilmad) and a 150 µL slug of the *Re*NHase solution were placed in the upper part of the EPR tube, about 3 cm from the top. The ∼1.5 cm slugs were quite stable in position due to capillary attraction to the tube walls. The EPR tube was allowed to thermally equilibrate in the −20 °C freezer for 30 min. The reaction was then initiated by holding the 25 cm-long EPR tube by the neck and violently flicking the tube to propel the contents to the bottom of the tube; this method has been observed to provide surprisingly efficient mixing. (25) For the shortest reaction times, the tube was immediately plunged into a bath of methanol on solid CO_2 with agitation.

For incubation times of >5 s, the mixing was carried out in the freezer compartment and the door was immediately closed afterward, with the remainder of the incubation (up to 30 s) carried out with the tube lying directly on the cold freezer floor. An accumulated layer of frost (∼3 mm) in the corrugations of the freezer floor provided good thermal contact with the sample, and the temperature of a control sample that remained in the freezer was stable within 1 °C throughout the procedure; however, the use of a bath of the temperature-equilibrated eutectic mixture, with a large heat coefficient and in which to incubate samples, could be employed where concerns around temperature stability exist.

Following freezing, the samples were stored either under liquid N_2 or at −80 °C prior to EPR examination. The samples were examined as soon as possible after generation as sample tubes tended to shatter upon handling that involved temperature changes (SCC solutions expand by 5% upon slow freezing (26) and the solid solution likely imposes significant stress on the tube upon rapid freezing); because of this, the use of a liquid nitrogen finger dewar for EPR that contained no salt-corrodible parts and is easy to clean in the event of tube failure was preferred for routine EPR studies of the low-spin Fe(III) signals over a variable-temperature cryostat.

EPR Spectroscopy

EPR spectra were obtained on an updated Bruker EMX-AA-TDU/L spectrometer equipped with an ER4112-SHQ resonator and an HP 5350B microwave counter for precise frequency measurement. Spectra were recorded with 5 G magnetic field modulation at 100 kHz at either 77 K (∼9.45 GHz) with 5 mW microwave power, 50 K with 2 mW microwave power, or either 25 or 35 K (∼9.49 GHz) with 0.5–5 mW microwave power; the conditions at 50 and 77 K were nonsaturating for low-spin Fe(III), and 0.5 mW at 25 K was only slightly saturating, whereas putative high-spin Fe(III) signals could be much better observed with 5 mW power at 25 K. A temperature of 77 K was maintained with liquid nitrogen, while temperatures of 25–50 K were maintained using a ColdEdge/Bruker Stinger S5-L recirculating helium refrigerator, an Oxford ESR900 cryostat, and MercuryITC temperature controller. EPR simulations were carried out using EasySpin, (27) and all spectra are presented on a field scale corresponding to a resonant frequency of 9.49 GHz. An integration standard of 1.7 mM Cu(II) in 50 mM HEPES buffer containing 15% v/v glycerol and 10 mM imidazole at pH 7.5 was prepared, and EPR spectra were recorded at 77 K, 0.5 mW. These data were used to calibrate spin densities from *Re*NHase EPR spectra with standard corrections for differences in $1/T$, $\sqrt{(\text{microwave power})}$, and (field range)^2.

Computational Methods

Density functional theory (DFT) calculations were performed using the ORCA 3.0 software package developed by Neese. (28) Unless otherwise noted, calculations utilized the PBE0 functional (i.e., the one-parameter hybrid version of the Perdew–Burke–Ernzerhof functional). (29,30) Ahlrichs' valence triple-ζ (TZV) basis sets with additional polarization functions on heavy atoms were employed in conjunction with the appropriate auxiliary basis set. (31,32) The truncated version of the Fe-NHase active site was based on previous computational studies by our group (14) and Hopmann. (20) In addition to the primary coordination sphere provided by the "claw-setting", these computational models included the two conserved protonated arginine residues (Arg56 and Arg141) capable of participating in hydrogen-bonding interactions with the Cys–SO^- and Cys–SO_2^- moieties. Energy-minimized active-site structures were generated by constrained geometry optimizations in which the positions of carbon atoms attached to the protein backbone were fixed. In addition to these geometry-optimized models, single-point calculations were also performed with Fe-NHase models reported by the Solomon, (17) Hopmann, (20) and Toscano (16) groups. Time-dependent DFT (TD-DFT) calculations (33−35) provided absorption energies and intensities for 40 excited states within the Tamm–Dancoff approximation. (36,37)

EPR *g*-values of the Fe-NHase active-site models were calculated using two different methodologies. The first approach, labeled "Taylor/DFT", is based on a set of equations developed by Taylor that describe the relationship between *g*-values, ligand-field parameters, and spin–orbit coupling (SOC) for low-spin Fe(III) systems. (38) In this approach, the tetragonal splitting (Δ) between the Fe d_{xy} orbital and d_{xz}/d_{yz} pair and the rhombic splitting (*V*) between the Fe d_{xz} and d_{yz} orbitals were computed using TD-DFT. The SOC parameter (λ_{Fe}) was fixed at 460 cm^{-1}–a value determined by calibrating this methodology to a series of nonheme Fe–S/N complexes with known *g*-values. (39) With these three parameters (Δ, *V*, λ_{Fe}) as inputs, the application of the Taylor equations yielded *g*-values for each of the Fe-NHase models in Figure 2. An important constraint is that the computed *g*-values were required to correspond to a normalized orbital, such that the sum of the squares of the coefficients for the Fe d_{yz}, d_{xz}, and d_{xy} orbitals are equal to one for the singly-occupied MO. Further details regarding the Taylor/DFT method are provided in our earlier report. (14)

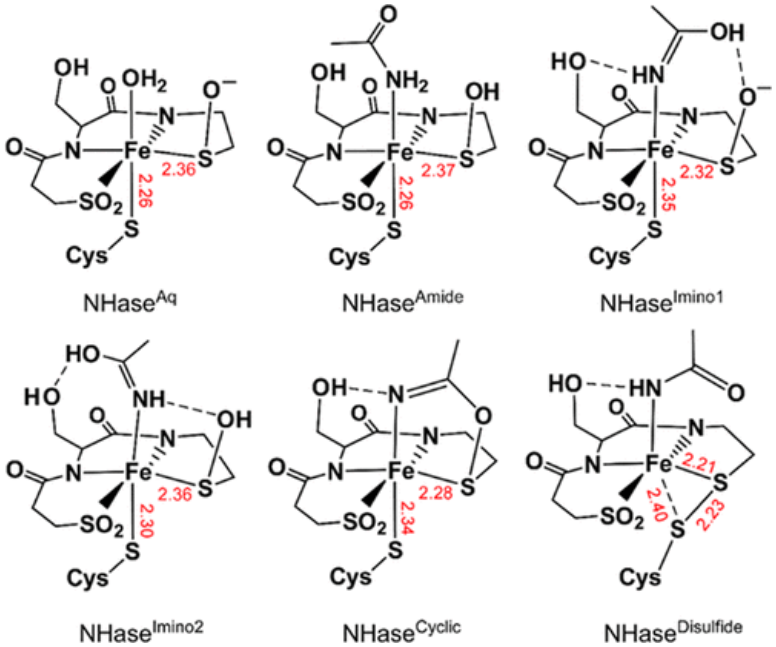

Figure 2. Structural models for calculations of *g*-values.

In the second approach, EPR *g*-values were calculated by applying complete active space self-consistent field (CASSCF)-based methods to select Fe-NHase models. (40,41) These calculations were performed using an updated version (4.0) of the ORCA software package. Valence triple-ζ Karlsruhe basis sets combined with polarization functions on the main group and transition-metal elements (def2-TZVP) were employed. (42) Single-point calculations of the Fe-NHase models employing the B3LYP functional (43,44) provided unrestricted natural orbitals that served as the initial guess for state-averaged CASSCF calculations. The CAS(5,5) active space consisted of five electrons in the five Fe 3d orbitals. The 10 lowest-energy doublet roots were calculated. Dynamic electron correction was incorporated using *N*-electron valence state second-order perturbation theory (NEVPT2). (45) Application of the effective Hamiltonian method to the multiconfigurational CASSCF/NEVPT2 wavefunctions yielded the computed *g*-values listed in Table S2 of the Supporting Information.

Results

Steady-State Kinetic Analyses

To establish a baseline for enzymatic activity, steady-state kinetic parameters for *Re*NHase were measured in 50 mM HEPES buffer at pH 7.5 and 25 °C with various substrates. As shown in Table 1, the activity with acrylonitrile, the most commonly reported substrate, was similar to the values previously reported. (14)

Table 1. Steady-State Kinetic Analysis of *Re*NHase at pH 7.5, 25 °C with Different Substrates

substrate[a]	k_{cat} **(s^{-1})**	K_m **(μM)**
benzonitrile	30.9 ± 1.5	13.2 ± 1.4
3-hydroxybenzonitrile	15.9 ± 1.6	77 ± 17
3,4-dihydroxybenzonitrile	1.5 ± 0.2	168 ± 21
acrylonitrile	620 ± 140	25 000 ± 11 000
acetonitrile	198 ± 11	25 000 ± 2000

[a]In 50 mM HEPES pH 7.5.

Characterization of Intermediate-Trapping Methodologies

The most common method for trapping enzyme reaction intermediates for subsequent spectroscopic analysis is rapid-freeze-quench (RFQ). In this approach, intermediates are generated by rapid mixing and freezing the mixture as a spray into a nominally immiscible, inert cryogen such as 2-methylbutane (2-MeBu; isopentane) at around −100 °C. Even though this methodology is well-established, attempts to generate RFQ samples of NHase for EPR studies proved difficult. Vigorous agitation of NHase for 2 min with 2-MeBu using a vortex mixer or manual shaking had only a minor impact on the EPR spectra of the resulting samples (Figure S1; traces A and B). However, over time in the presence of 2-MeBu, the enzyme color changed from green to brown and the activity fell to <1%. Analogous results were observed with 2-methylpentane and *n*-pentane. Upon mixing the enzyme as a spray with cold 2-MeBu, using the RFQ apparatus, changes to the EPR spectrum were more dramatic, with both slow- and fast-relaxing signals that spanned the 4000 G field range of the EPR spectrum. Thawing and refreezing this mixture led to further changes in the spectrum and, finally, complete loss of the signals (Figure S1; traces D and E). Over three sets of experiments, the precise nature of the altered EPR signals differed quantitatively in terms of resonance positions and intensities but was qualitatively similar. An alternative approach of using a DMSO eutectic system (24) was also found to be unsuitable, as NHase exposed to 50% DMSO was completely inactive, even when subsequently diluted in aqueous buffer to very low DMSO concentrations.

The activities of NHase in the 23% (w/w) $NaCl/H_2O$ eutectic system at pH values from 5.0 to 10.0 were found to be between 2% (at pH 10.0) and 56% (at pH 7.5) of those in unsalted buffers at the same respective pH values

(Table 2). Analysis of the temperature dependence of *Re*NHase activity at pH 7.5 toward acetonitrile (Figure S2) yielded a linear relationship, $\ln k_{\mathrm{cat}}\,(\mathrm{s}^{-1}) = -\frac{3810}{T\{\mathrm{K}\}} + 17.6$, predicting a k_{cat} value at −20 °C of ∼12 s^{-1}, i.e., a turnover time of about 80 ms. Using acetonitrile as the substrate, *Re*NHase exhibited a k_{cat} value of 111 ± 4 s^{-1} in the cryogenic salt solution (CSS) in 32.5 mM HEPES buffer at 25 °C, pH 7.5 compared to a k_{cat} value of 198 ± 11 s^{-1} in the absence of 23% NaCl (Table 2). The k_{cat} values for *Re*NHase with acetonitrile in eutectic CSS solutions with MES pH 5.0, CHES pH 9.0, CHES pH 9.5, and CHES pH 10.0 (CSS 5.0, CSS 9.0, CSS 9.5, and CSS 10.0, respectively) varied from about 2% of that in the corresponding unsalted buffer at pH 10, to almost 50% at pH 7.5 (Table 2).

Table 2. Comparison of k_{cat} for *Re*NHase with Acetonitrile at 25 °C in NaCl-Free Buffer and in 23% (w/w) NaCl/H_2O Eutectic CSS Solutions

pH	k_{cat} no NaCl	k_{cat} in CSS
5.0	160 ± 15	10 ± 5
7.5	198 ± 11	111 ± 4
9.0	170 ± 7	21 ± 1
9.5	110 ± 6	5 ± 1
10.0	64 ± 3	1.0 ± 0.1

The “lost” activity of the enzyme in CSS 7.55 was entirely recoverable upon exchange into unsalted buffer, allowing for recycling of enzyme so long as exposure to air was minimal. The observed activity in CSS 7.5 of 56% relative to that in unsalted buffer was in reasonably good agreement from that predicted from the application of Kramers’ theorem (46) to diffusional processes in proteins and enzymes (47,48) and, specifically, to enzyme activity in which the rate-limiting step is a diffusion process. (49,50) Briefly, the dynamic viscosity, μ, of 4 M (23.3%) NaCl at 20 °C is 1513 μPa s compared to 1002 μPa s for water, (51) and the reaction rate, k, obeys $k \propto \mu^{-1}$, which predicts the activity in CSS 7.5 to be around 65% of that in unsalted buffer. (50) The viscosity of NaCl solutions is also linearly inversely proportional to the absolute temperature over the range that is relevant here, i.e., $\Delta T \approx 40$ K, (51) and thus the temperature dependence of viscosity effects on the activity at −20 °C are inherently accounted for in the empirical Arrhenius analysis of temperature dependence. The kinetic parameter space encompassing k_{cat} and K_{m} as functions of [NaCl], temperature, and pH is large, and a detailed systematic study, while warranted, is outside the scope of the present investigation.

The total reaction time for the cryoenzymological trapping method is given by the sum of three factors: (i) the time required to mix the enzyme and the substrate, (ii) the time to transfer to the cold bath, and (iii) the time it takes to freeze the sample. By comparing this overall reaction time to the turnover time derived from kinetic assays and Arrhenius analysis, it is possible to determine whether the reaction time for various amounts of substrate lies in the presteady state or the steady state, or whether the substrate has been exhausted by the time the sample is frozen. The shortest reproducible combined time of mixing and sample transfer to cold acetone was standardized by a calibrated manual count (“bartender’s count”) of approximately one second. Applying Newton’s law of cooling to calculate the freezing time, however, indicated that the latter is not a straightforward quantity to determine. The sample itself is a eutectic system, and the spherulite model investigated in earlier studies of the freezing of protein solutions does not, therefore, apply. (52) Another complication is that although the sample is transferred to the −78 °C bath at −20 °C, which is only −2 °C above the freezing point, the eutectic mixture can exist as a supercooled liquid to −30 °C; this phenomenon is, perhaps surprisingly and in contrast to pure water, reported to be insensitive to the nucleation environment. (53) At −30 °C, crystallization of the supercooled eutectic occurs essentially instantaneously, abruptly halting any enzymatic reaction, with subsequent liberation of the latent heat of fusion from the immobile, frozen solution. Finally, given the geometry of the sample and the anticipated short time of freezing, convection can be neglected; this,

inconveniently, precludes the use of engineering standard tables that are used for larger and/or flowing systems. The parameter space from which to calculate the freezing profile of the sample is large, but a model example is highly illustrative. Taking the fused quartz sample tube alone, immersion into −78 °C lowers the temperature of the tube from −20 to −52 °C in 0.2 s. Then, considering the 50% (150 μL) of the sample closest to the inside of the tube as a cylinder of outside diameter of 3 mm and inside diameter of 1.52 mm, the mean sample temperature is reduced to the supercooled-freezing temperature of −30 °C in 0.36 s. This assumes a steady tube temperature of −52 °C; in fact, the cooling constant for the tube is about 4-fold higher than for the sample, so the freezing time of 0.36 s is an upper limit in this model.

During the cooling-to-freezing time of 0.36 s, application of the Arrhenius equation suggests that 1.0 turnover occurs with acetonitrile at pH 7.5 during freezing of the outer half of the sample. In addition, 14.4 turnovers occur during the combined incubation and transfer times (of 1 s), resulting in a total of 15.4 turnovers prior to sample freezing. Cooling of the entire sample to −30 °C, on the other hand, takes 1.7 s, corresponding to 19.1 turnovers. This analysis assumes that a temperature gradient across the sample exists and is supported by the calculation of a Biot number for the sample of 0.72, significantly higher than the value of 0.1, which would indicate only a 5% deviation from uniform temperature. (54) The Biot number for the frozen sample is 0.71, and that for the quartz tube is 0.97, which indicates that the net rate of heat transfer through the sample-and-tube structure and the heat transfer rate out through the structure surface is about equal. The thermal conductivity of ice is ∼4.6× those of supercooled water (−20 °C) and the NaCl/H_2O eutectic, respectively, indicating that the favored conduit for the escape of latent heat of fusion released by the nascent frozen solution is through the frozen sample to the outside low-temperature reservoir via the quartz tube rather than into the remaining supercooled liquid sample. (55)

This analysis, then, predicts that the number of turnovers of acetonitrile at pH 7.5 that occur during the shortest available total reaction time follows a distribution of ∼15 ± 4 turnovers. Thus, this situation clearly precludes the trapping of presteady-state intermediates with acetonitrile at pH 7.5, for example. However, steady-state intermediates can be trapped using the methodology, with 10–20 equiv of acetonitrile. In principle, presteady-state intermediates could be trapped with acetonitrile at pH 9.5 or 10.0, though the wide distribution in reaction times across the sample would require unusually long-lived presteady-state intermediates to accumulate in concentrations amenable to EPR detection.

EPR-Spectrokinetic Studies at pH 7.5 Using the Salt-Water Eutectic System

At pH 7.5, the EPR spectrum of the as-prepared *Re*NHase in the 23% NaCl CSS at pH 7.5 (Figure 3; trace A) is almost indistinguishable from that obtained in unsalted HEPES buffer, pH 7.5 (Figure S1; trace A). In both cases, the EPR spectrum could be simulated as a mixture of *Re*NHase species where the active species ($NHase^{Aq}$) is the predominant type (∼63%). As described previously, the $NHase^{Aq}$ species features an Fe-bound H_2O molecule in the axial position, as illustrated in Figure 2. In the present work, the g_1-value of $NHase^{Aq}$ is shifted slightly to 2.197 from the previously reported value of 2.206 in unsalted HEPES buffer. The second major contributor to the as-prepared spectrum is $NHase^{Ox}$ (∼22%), in which the Cys–SO ligand has been further oxidized to Cys–SO_2. (8) Finally, 15% of the overall signal is due to uncharacterized species, denoted $NHase^{NA1}$ (NA = not assigned). The *g*-values and spin contributions for each of the species contributing to the most mechanistically relevant EPR spectra presented herein are given in Table 3, and a more comprehensive list is given in Table S1.

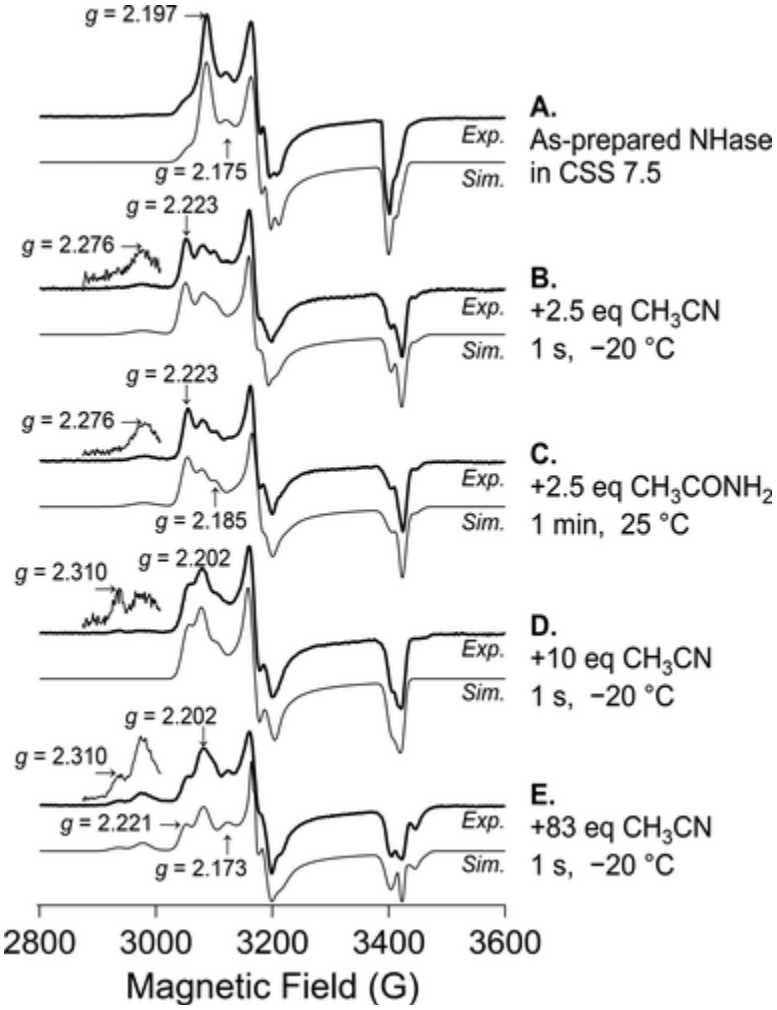

Figure 3. EPR spectra of (A) as-prepared *Re*NHase, (B) 2.5 equiv of ACN added to *Re*NHase, (C) 2.5 equiv acetamide added to *Re*NHase, (D) 10 equiv of ACN added to *Re*NHase, and (E) 83 equiv of ACN mixed with *Re*NHase, recorded at 25 K. Samples prepared in 12 mM HEPES, 23% (w/w) NaCl/H_2O, pH 7.5. (Exp; experimental EPR spectrum, Sim; computer simulation of experimental EPR spectrum.).

Table 3. Simulation-Derived Experimental *g*-Values and Spin Fractions for EPR Spectra from *Re*NHase

sample	spectrum (figure, trace)	experimental EPR species[a]	g_1	g_2	g_3	spin-density fraction
resting	Figure 3A	$NHase^{Aq}$	2.197	2.136	1.994	0.63
CSS 7.5		$NHase^{Ox}$	2.175	2.124	1.986	0.22
		$NHase^{NA1}$	2.218	2.115[b]	1.981[b]	0.15
acetonitrile, 2.5 equiv	Figure 3B	$NHase^{Prod2}$	2.276	2.128[b]	1.973[b]	0.06
1 sc at –20 °C		$NHase^{Prod1}$	2.223	2.139	1.971	0.47
CSS 7.5		$NHase^{Aq}$	2.201	2.130	1.991	0.30
		$NHase^{NA2}$	2.185	2.118[b]	1.973[b]	0.17
acetonitrile, 83 equiv	Figure 3E	$NHase^{INT}$	2.310	2.136	1.960	0.05
1 sc at –20 °C		$NHase^{Prod2}$	2.278	2.130[b]	1.976[b]	0.12
CSS 7.5		$NHase^{Prod1}$	2.221	2.139	1.975	0.23
		$NHase^{Aq}$	2.202	2.127	1.992	0.45
		$NHase^{Ox}$	2.173	2.120	1.986	0.15

[a]NHase^{Aq}, active uncomplexed NHase; NHase^{Ox}, oxidized inactive uncomplexed NHase; NHase^{NA1}, not assigned to a defined chemical species; NHase^{Prod2}, NHase noncovalent complex obtained upon direct addition of acetamide; NHase^{Prod1}, NHase product-complex with acetamide following the reaction with acetonitrile; NHase^{INT}, proposed catalytically competent intermediate with acetonitrile; NHase^{NA2}, not definitively assigned but possibly due to product bound as the amide tautomer.
[b]These resonances could not be observed directly, and the *g*-values for these were obtained from the best fit to the overall simulation; they should therefore be treated with caution.
[c]The indicated time is for incubation prior to immersion in acetone at −78 °C and does not include the time-to-freezing.

The reaction of *Re*NHase with 2.5 equiv acetonitrile for 2 s at −20 °C yields an EPR spectrum that is indistinguishable from the product complex obtained by the direct addition of 2.5 equiv of acetamide (Figure 3; traces B and C). This result is not surprising given our prior analysis that ∼15 ± 4 turnovers occur during the mixing-transfer-freezing time of the NaCl/H_2O eutectic solution, meaning that all of the added substrates are converted to products (vide supra). Each of the spectra B and C consist of at least four distinct signals, as evidenced by four distinct g_1 resonances that are clearly observable at magnetic fields of 2975, 3050, 3080, and 3100 G. Intensity from NHase^{Aq} is still observed (g_1 = 3080 G), but now it only accounts for about one-third of the spin density. The newly predominant signal, exhibiting ∼50% of the spin density, exhibits a g_1-resonance at 3050 G. Its features are quite similar to those observed in earlier work upon the addition of acetonitrile to *Re*NHase, (14) as well as a signal detected upon the addition of acetonitrile to intact *Re*NHase-expressed in *E. coli*. (23) In the present work, the signal with g_1 = 3050 is labeled NHase^{Prod1} to indicate that it arises from a product-bound complex. The most anisotropic signal in spectra B and C, which was also observed in the earlier work, (23) accounts for <10% of the total spins and exhibits a g_1-value of 2.276 (i.e., the peak at 2975 G). This signal is very similar to the one displayed by the reversibly inhibited noncovalent complex of NHase with butyric acid, NHase^{BA} (g_1 = 2.281). (14) Therefore, we tentatively assign the g_1 = 2.276 signal (labeled NHase^{Prod2}) to a species where acetamide is present in the active-site pocket but in a different position or orientation than NHase^{Prod1}. Both the NHase^{Prod1} and NHase^{Prod2} signals are elicited upon direct addition of either acetonitrile or the reaction product (acetamide), confirming their assignments as product-bound species. Likely structures for NHase^{Prod2} and NHase^{Prod2} are discussed in the DFT computational section below. The balance of the spin density was accounted for by a signal with g_1 ≈ 2.185 (labeled NHase^{NA2}). The nature of this species is ambiguous, although DFT calculations suggest a possible origin.

Upon reaction with a higher concentration of acetonitrile (10 equiv), an EPR spectrum was observed (Figure 3; trace D) whose appearance is clearly different from that of the resting enzyme, as well as of the product-complexed species in traces A–C. As noted above, the kinetic data predict a mean turnover number of about 15 prior to sample freezing in the NaCl/H_2O eutectic solution. However, the large variation about this value and uncertainties arising from the approximations and/or models employed in the analysis itself leave open the possibility that a significant fraction of the sample may have frozen before 10 turnovers, i.e., during the steady state. Indeed, the striking differences between traces B and D (Figure 3) strongly suggest that the reaction may not have gone to completion, at least not for the entire sample. The high-amplitude central part of trace D (between 3020 and 3420 G) is largely accounted for by NHase^{Prod1} (38%) and the active NHase^{Aq} species (47%), with the balance of spin density in that region likely due to NHase^{NA2}. To the low-field of the central region of the spectrum, the resonance at 2975 G due to NHase^{Prod2} was also evident, although it was not included in the simulation. Most significantly, a heretofore unobserved and highly rhombic signal with *g*-values of 2.310, 2.136, and 1.960 is observed. This signal is denoted as NHase^{INT}. The g ∼2.31 and 2.28 features of NHase^{INT} and NHase^{Prod1}, respectively, are much more intense in an EPR spectrum obtained after reaction with 83 equiv of acetonitrile (Figure 3; trace E). The reaction mixture of the latter was frozen well before the expected time for

exhaustion of the substrate (roughly 6.6 s). The central region of the spectrum was again simulated using known species, predominantly NHase^{Aq} (45%), along with NHase^{Prod1} (23%) and a small amount of an oxidized species (NHase^{Ox}). The NHase^{INT} signal accounts for 5% of the total spin intensity, indicating that only small amounts of this intermediate are present under steady-state conditions. Possible structures for NHase^{INT}, NHase^{Prod1}, NHase^{Prod2}, and NHase^{NA2} are presented in the computational section below.

Additional studies were carried out with the much slower substrate benzonitrile. Differences in the EPR spectrum were observed upon incubation of NHase with benzonitrile, but there was little evidence for an intermediate. Furthermore, a lack of knowledge of the solubility of benzonitrile in CSS 7.5 at −20 °C precluded any solid rationalization of the results, which are presented and described in the Supporting Information (Figure S3).

EPR-Spectrokinetic Studies with Acetonitrile at pH 5 and 10 Using the Salt–Eutectic System

In another attempt to capture *Re*NHase reaction intermediates, *Re*NHase was reacted with 2.5 equiv of acetonitrile at pH 5 and 10 at −20 °C. Under these conditions, the steady state would be expected to persist for 3.3 and 12.8 s, respectively, well beyond the predicted lower limit of the NaCl/H_2O eutectic cryoenzymology technique. At pH 5.0, the presence of a signal at 2976 G ($g_1 \sim 2.278$) suggests that the buffer sulfonic acid mimics butyric acid in binding in the substrate-binding site as the latter gives rise to a feature at $g_1 \sim 2.281$. (14) The key finding, however, is that the lowest-field signal with g_1 at 2.31 is again elicited upon trapping the steady state (Figure 4; trace B). Upon longer reaction time of 30 s, about 2.5 times the expected characteristic lifetime of the steady state, the g = 2.31 resonance is all but undetectable, establishing the kinetic competence of the signal. Furthermore, the direct addition of acetamide to NHase in CSS 5.0 failed to elicit the g = 2.31 signal. At pH 10.0, no catalytically competent signals were observed, and the only additional signals correspond to NHase^{Prod1} (Figure S4).

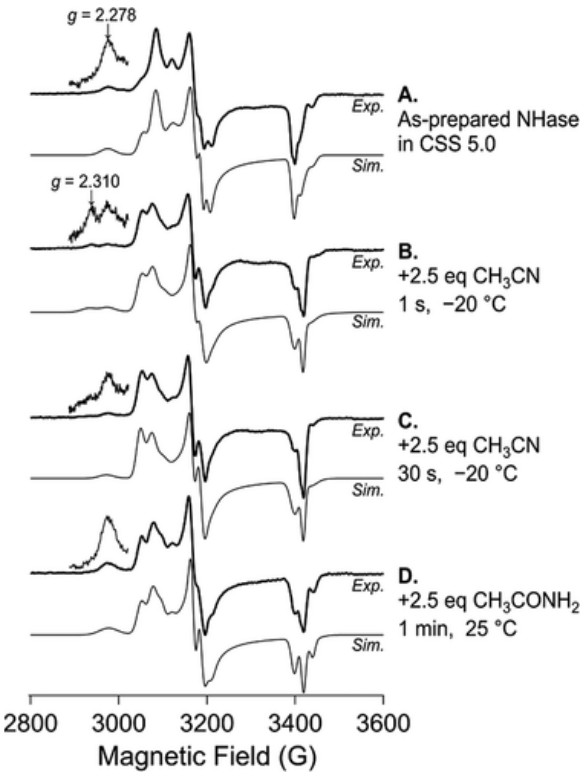

Figure 4. EPR spectra of (A) as-prepared *Re*NHase, (B) 2.5 equiv of ACN added *Re*NHase, frozen after 2 s, (C) 2.5 equiv ACN added *Re*NHase, frozen after 30 s, and (D) 2.5 equiv acetamide added *Re*NHase, recorded at 25 K. The

samples were prepared in CSS 5.0 NaCl/H_2O eutectic buffer. (Exp; experimental EPR spectrum, Sim; computer simulation of experimental EPR spectrum.).

EPR *g*-Value Calculations

Computational methods provided additional insights into the geometric and electronic structures of *Re*NHase species observed by EPR spectroscopy. Active-site models were generated via constrained DFT geometry optimizations of proposed intermediates in the Fe-NHase catalytic cycle. The EPR *g*-values of the resulting models were then computed and compared to the experimental data. DFT calculations have difficulty treating the unquenched orbital angular momentum of low-spin Fe(III) centers, which arises from the parent $^2T_{2g}$ ground state in O_h symmetry. Because of this shortcoming, DFT methods often underestimate the **g**-tensor anisotropy of low-spin Fe(III) EPR signals. Thus, we previously (14) developed an alternative approach that employs a set of equations developed by Taylor (27) and Griffith (56) for low-spin ferric heme complexes. In this hybrid approach, the energy splitting between the three $^2T_{2g}$-derived states is obtained from time-dependent DFT calculations. More recently, we used the complete active space self-consistent field (CASSCF) method, in conjunction with *n*-electron valence state second-order perturbation theory (NEVPT2), to compute accurate *g*-values for cyanide-treated cysteine dioxygenase (CDO) and related model complexes. (57) We have applied both the Taylor/DFT and CASSCF/NEVPT2 methods to structural models of $NHase^{Aq}$ and $NHase^{BA}$. As summarized in Table S2, the Taylor/DFT approach better reproduces the experimental *g*-values, as the CASSCF/NEVPT2 calculations far overestimate the **g**-tensor anisotropy. This result is perhaps not surprising, given that our Taylor/DFT approach was calibrated using low-spin Fe(III)–S/N complexes that closely resemble the Fe-NHase active site. Thus, the remainder of this section will focus on *g*-values calculated using the hybrid Taylor/DFT procedure.

Our initial efforts examined possible structures of the product-bound enzyme, which can be generated by either incubation of $NHase^{Aq}$ with the substrate acetonitrile or by the direct addition of acetamide to $NHase^{Aq}$ (vide supra). Three possible structures were considered as models. In the first structure, labeled **$NHase^{Amide}$** in Figure 2, acetamide coordinates to the Fe(III) center via its $-NH_2$ unit (note: to distinguish between these DFT models and the EPR signals identified above, the labels for computational models are provided in **bold text**). In the second and third structures, **$NHase^{Imino1}$** and **$NHase^{Imino2}$**, the product coordinates to Fe(III) in its iminol tautomeric form (Figure 2)–a possibility suggested by Solomon and co-workers in an earlier study. (17) Tautomerization allows the product to engage in H-bonding interactions with both the sulfenate (SO) ligand and the −OH group of the nearby Ser side-chain. The H-bonding pairs differ in the **$NHase^{Imino1}$** and **$NHase^{Imino2}$** structures due to the ∼180° rotation of the product around the $Fe–N_{iminol}$ axis (Figure 2). The iminol-containing structures feature $Fe–N_{iminol}$ bond distances near 2.03 Å. This value is considerably shorter than the $Fe–N_{acetamide}$ bond distance of 2.336 Å in the **$NHase^{Amide}$** structure. Thus, the DFT results suggest that tautomerization to the iminol form stabilizes the enzyme–product complex, whereas the amide tautomer binds rather weakly to the Fe(III) center.

Table 4 summarizes the EPR *g*-values calculated for various Fe-NHase models using the hybrid Taylor/DFT approach. As reported previously, these calculations accurately reproduce the experimental *g*-values of the resting enzyme, $NHase^{Aq}$, and this species serves as a useful benchmark for evaluating shifts in *g*-values. The computed *g*-values for **$NHase^{Amide}$** and **$NHase^{Aq}$** are nearly identical, whereas the iminol-containing structures yield **g**-tensors that are notably more anisotropic (as indicated by the $g_1 – g_3$ parameter in Table 4). Indeed, the *g*-values calculated for **$NHase^{Imino2}$** (Table 4) are remarkably similar to those measured for the $NHase^{Prod1}$ signals in the experimental EPR spectra of acetamide-treated *Re*NHase. The calculated values for **$NHase^{Imino1}$** are similar to those calculated for **$NHase^{BA}$**, and the experimental values for the physical species to which these models correspond ($NHase^{Prod2}$ and $NHase^{BA}$, respectively) are also very similar though, in both cases, the calculations underestimate g_1 by about 0.035. At pH 7.5, the experimental signal corresponding

to **NHase^{Imino1}** was only observed upon addition of acetonitrile or acetamide and the intensity was sensitive to the amount added, establishing the origin of the NHase^{Prod2} signal as being acetamide-dependent (Figure 3B,C). Thus, the combined EPR and computational results suggest that the acetamide product binds to the NHase active site as its iminol tautomer, perhaps in two different orientations (**NHase^{Imino1}** and **NHase^{Imino2}**). Conversion to the amide tautomer likely yields a species with EPR parameters similar to NHase^{Aq}. This species may correspond to the NHase^{NA2} signal that was only observed upon exposure to acetonitrile/acetamide and not in the resting enzyme.

Table 4. Taylor/DFT-Computed EPR *g*-Values for Fe(III)–*Re*NHase Intermediates

NHase state	computational model	g_1	g_2	g_3	$(g_1 - g_3)$
resting enzyme	NHase^{Aq}	2.215	2.117	1.979	0.236
butyric acid bound[a]	NHase^{BA}	2.248	2.121	1.970	0.278
product-bound	NHase^{Amide}	2.214	2.116	1.977	0.237
enzyme	NHase^{Imino1}	2.241	2.133	1.970	0.271
	NHase^{Imino2}	2.232	2.123	1.973	0.259
cyclic	NHase^{Cyclic}	2.169	2.102	1.984	0.185
intermediate	NHase$^{Cyclic\ (Solomon)}$ b	2.162	2.098	1.986	0.176
	NHase$^{Cyclic\ (Hopmann)}$ c	2.171	2.106	1.983	0.188
disulfide	NHase^{Disulfide}	2.177	2.109	1.982	0.195
intermediate	NHase$^{Disulfide\ (Hopmann)}$ d	2.153	2.109	1.985	0.168
	NHase$^{Disulfide\ (Toscano)}$ e	2.264	2.113	1.969	0.295

[a]Structural modes are proposed from the present work (Figure 2), except for the structural model for NHase^{BA}, which is from ref (14).
[b]The structural model for NHase$^{Cyclic\ (Solomon)}$ is derived from ref (17).
[c]The structural model for NHase$^{Cyclic\ (Hopmann)}$ is derived from ref (20).
[d]The structural model for NHase$^{Disulfide\ (Hopmann)}$ is derived from ref (20).
[e]The structural model for NHase$^{Disulfide\ (Toscano)}$ is derived from ref (16).

We also sought to identify the origin of the experimental g = 2.31 signal (NHase^{INT}) by calculating g-values for several proposed intermediates in the Fe-NHase catalytic cycle. As illustrated in Figure 1, nucleophilic attack of the sulfenate (SO) ligand on the coordinated nitrile substrate is presumed to yield a cyclic intermediate (**NHase^{Cyclic}**). Our calculations predict that the cyclic intermediate will exhibit a g_1-value near 2.17, and the overall **g**-tensor is less anisotropic than the one computed for **NHase^{Aq}**. Similar sets of g-values are obtained if computational models of the cyclic intermediate from studies by Solomon (17) and Hopmann (20) are employed (Table 4). Thus, based on our results, it appears unlikely that any of the signals with low-field g_1 resonances arise from **NHase^{Cyclic}**.

Protonation of the substrate-derived *N*-atom of the cyclic intermediate results in spontaneous cleavage of the S–O bond upon geometry optimization, yielding a coordinated amidate ligand. Because this process is accompanied by the formation of a disulfide bond between two Cys residues, the resulting model is labeled **NHase^{Disulfide}** in Figure 2. Similar disulfide structures have been proposed as intermediates or transition states in earlier computational studies. (16−18,20) In our structure, the disulfide unit exhibits monodentate coordination via the S-atom cis to the substrate-derived amidate (see bond distances in Figure 2), similar to Hopmann's model. (20) In contrast, the disulfide ligand in the model reported by Toscano et al. (16) binds in a more symmetric manner with comparable Fe–S bond distances of 2.33 and 2.40 Å. As shown in Table 4, the g-values computed for our disulfide model (as well as Hopmann's) are not dissimilar to those obtained for **NHase^{Aq}** and **NHase^{Acet}**. However, those computed for Toscano's **NHase^{Disulfide}** model are considerably more anisotropic with a g_1-value of 2.264, which is larger than the g_1-value of 2.24 computed for **NHase^{Imino1}**. Indeed,

the computed *g*-values for Toscano's **NHase^{Disulfide}** model are the most rhombic and anisotropic of any NHase model considered here. While far from conclusive, this result suggests that a disulfide-containing intermediate might be responsible for the observed NHase^{INT} signal with g_1 = 2.31. Based on reaction profiles computed previously, this species undergoes subsequent reaction with H_2O to protonate substrate and regenerate the −SO ligand, but the high energy of the transition barrier suggests that trapping the disulfide intermediate is feasible. (16,18,20)

The NHase^{INT} signal was only observed during the steady state and was extinguished at the exhaustion of the substrate, usually an indicator of catalytic competence of the responsible species and in support of the assignment of the species to an intermediate along the catalytic pathway. However, the unavoidable presence of some inactive NHase^{Ox}, which is generated in vivo prior to enzyme isolation, (23) allowed for an alternative explanation in which the NHase^{INT} signal is due to binding of the acetonitrile substrate to inactive NHase^{Ox}. In that case, and if acetonitrile were only weakly bound to NHase^{Ox}, then the signal would persist only until the substrate had been exhausted. This possibility was particularly intriguing because it raised the possibility that the species may be a good analogue of the Michaelis complex of the catalytic pathway. Taylor/DFT calculations were therefore carried out on the acetonitrile complex of NHase^{Ox}, in which acetonitrile replaced the axial water ligand and was bound to iron via the nitrile nitrogen atom. The calculations returned *g*-values of 2.217, 2.127, and 1.975, which are essentially indistinguishable from those of water-bound NHase^{Ox}, 2.219, 2.111, and 1.976. (14) It seems highly unlikely, therefore, that the NHase^{INT} signal arises from an acetonitrile complex of NHase^{Ox} and the available evidence is more consistent with a catalytic intermediate.

Discussion

The principal aim of this study was to capture intermediates in the catalytic cycle of *Re*NHase for analysis with EPR spectroscopy. Initial efforts to trap presteady-state species using traditional RFQ techniques were unsuccessful as the requisite cryogenic solvents resulted in enzyme inactivation. We also attempted to perform the reaction at a very low temperature (−80 °C) in a suitable eutectic mixture to slow the reaction to the point where presteady-state intermediates could be trapped by manual freezing. Unfortunately, neither approach was amenable to NHase. Degradation of NHase in 2-MeBu was extremely rapid under the conditions of RFQ, in which a very fine spray of reactant solution is squirted into a bath of cooled 2-MeBu at very high velocity. A possible explanation is that hydrophobic interactions along the αβ dimer interfaces may be highly susceptible to disruption by the hydrophobic or aprotic solvents employed in RFQ methods.

In contrast, the use of a cryohydratic NaCl/H_2O eutectic mixture at −20 °C did allow for the trapping of NHase-substrate reaction mixtures during the steady state for examination by EPR, and new insights into the catalytic mechanism were obtained in conjunction with DFT. The most exciting finding was the emergence of a new EPR signal (NHase^{INT}) that has not been observed during earlier studies (14) or reported elsewhere. The NHase^{INT} signal was observed only in samples in which the catalytic reaction (here, with acetonitrile) was arrested by freezing while in the steady state; it was not observed in the resting enzyme, in reaction mixtures in which the substrate had been exhausted, or upon direct addition of the reaction product to the enzyme. The NHase^{INT} signal, which accounts for approximately 5% of the total spin, is distinguished by a g_1-value of 2.310–the highest *g*-value yet reported for a low-spin Fe(III) signal from NHase. Indeed, the NHase^{INT}**g**-tensor is the most anisotropic ever measured for NHase with a Δ*g*-value of 0.35 ($\Delta g = g_1 - g_3$). The NHase^{INT} signal is observed at the catalytically optimum pH of 7.5, as well as pH of 5.0. It is absent from samples prepared at pH 10.0. Additional signals were observed in the *g* = 2.25–2.28 region and were deconvoluted from the time-dependent EPR spectrokinetics; however, in contrast to the NHase^{INT} signal, these features also appear upon addition of the acetamide product. Two of these signals (NHase^{Prod1} and NHase^{Prod2}) were previously observed but poorly characterized in terms of both origin and EPR parameters. These signals are similar to those observed

when butyric acid was employed as an antioxidation prophylactic during earlier isolation procedures, and they are provisionally assigned to species in which the product binds to the Fe center as its iminol tautomer.

DFT calculations provided structural information on the newly observed and/or newly characterized EPR signals from *Re*NHase. The structural models are shown in Figure 2 or otherwise previously reported (Table 4) represent the consensus of likely reaction intermediates that are consistent with the converging mechanistic proposals for the NHase reaction cycle (Figure 1). (14,16,17,20) Calculations examined the possibility that the acetamide product is bound as the iminol tautomer in two slightly different configurations. The resulting models provided *g*-values that were strikingly similar to the experimental values of NHase^{Prod1} and NHase^{Prod2}, providing further evidence that these signals arise from the product-bound active site. Product release is the rate-limiting step of the NHase reaction with acetonitrile, and this finding suggests that the tautomerization of the NHase iminol complex to the amide complex precipitates product release. This hypothesis is supported by the **NHase^{Amide}** structural model in which the amide product is weakly bound to the Fe center. Notably, the calculated EPR parameters are close to those of the resting enzyme, indicating that the binding of acetamide is comparable to H_2O coordination. Interestingly, this finding may also suggest that the determination of initial metal coordination of the nitrile substrate at the apical axial position may be difficult to determine by EPR alone.

Of the structural models considered, none satisfactorily reproduced the anisotropy or high g_1-value of the experimentally characterized NHase^{INT} species, which represents the first, and only, kinetically competent species that has been observed in NHase. DFT calculations evaluated various structural models for the obligatory cyclic intermediate, **NHase^{Cyclic}**, in the consensus mechanism (Figure 2). These calculations returned *g*-values far removed from those of NHase^{INT} (Table 4). Thus, while **NHase^{Cyclic}** may be present in experimental spectra, it has not, as yet, been resolved from other spectral features. The interpretation of DFT models that feature a disulfide S–S bond between the axial cysteine ligand and the equatorial cysteine–sulfenic acid ligand is less clear. Two models derived from previous theoretical studies by Toscano and Hopmann (16,20) provide divergent *g*-values and a third, developed as part of this work (**NHase^{Disulfide}**; Figure 2), provided values similar to the Hopmann-derived model. The EPR parameters (Table 4) derived from these models perhaps allow for the possibility that the catalytically competent NHase^{INT} species may include some S–S bonding, especially given that our computational approach seems to slightly underestimate g_1-values. Regardless, the data are far from convincing and suggest a higher degree of subtlety in the electronic structure of the intermediate than has yet been considered by theoretical approaches to date.

In summary, the present study has discovered, by a novel EPR-spectrokinetic method for an enzyme unsuited to traditional rapid-quench, the first catalytically competent species in the reaction of a nitrile hydratase with a substrate. DFT calculations indicate that it is unlikely that this species corresponds to any of the heretofore proposed “obligatory” intermediates and, in particular, does not correspond to the consensus cyclic intermediate (**I** in Figure 1). However, the combined DFT/EPR results provide the first tentative experimental support for a transient S–S interaction at the active site during catalysis. Almost certainly, the results show that hitherto proposed structural models are naïve and that additional outer-sphere moieties may need to be included in structural models to better understand the associated geometric and electronic structures. Finally, EPR and DFT have shed significant light on the product release–the final and rate-limiting step of the reaction. Our results indicate that, at the conclusion of the reaction, the product of nitrile hydration exists as an iminol tautomer that is stabilized by hydrogen-bonding interactions to outer-sphere residues in the active site, including one of the previously nucleophilic cysteine–sulfenic oxygen atoms. Tautomerization to the amide form disrupts these hydrogen-bonding interactions and lengthens the Fe–N bond, thereby precipitating product release.

Supporting Information

The Supporting Information is available free of charge at https://pubs.acs.org/doi/10.1021/acs.biochem.1c00574.

- EPR spectra of NHase upon manual and rapid-quench mixing with isopentane; temperature dependence of NHase activity with acetonitrile at pH 7.5 from 5 to 35 °C; EPR-spectrokinetic characterization of NHase with benzonitrile at pH 7.5 and −20 °C; EPR-spectrokinetic characterization of NHase with acetonitrile at pH 10.0 and −20 °C; *g*-values and spin densities of paramagnetic species that contribute to the EPR signals from NHase upon reaction with acetonitrile; comparison of experimentally determined *g*-values of NHase EPR species with those calculated from structural models using the CP-CSF, Taylor/DFT, and CASSCF/NEVPT2 methods (PDF)

Accession Codes

Active NHase is an $\alpha_2\beta_2$ heterotetramer. The UniProtKB accession number for the iron-containing α-subunit of NHase from *Rhodobacter* sp. is Q53118, and that for the β-subunit is Q53117. There are no specific accession numbers for NHase from *R. equi*.

Terms & Conditions

Author Information

- **Corresponding Authors**
    - **Adam T. Fiedler** - *Department of Chemistry, Marquette University, 1414 West Clybourn Street, Milwaukee, Wisconsin 53233, United States*; https://orcid.org/0000-0002-6114-8557; Email: adam.fiedler@marquette.edu
    - **Richard C. Holz** - *Department of Chemistry, Marquette University, 1414 West Clybourn Street, Milwaukee, Wisconsin 53233, United States*; *Department of Chemistry, Colorado School of Mines, Golden, Colorado 80401, United States*; https://orcid.org/0000-0001-6093-2799; Email: rholz@mines.edu
    - **Brian Bennett** - *Department of Physics, Marquette University, 1420 West Clybourn Street, Milwaukee, Wisconsin 53233, United States*; https://orcid.org/0000-0003-2688-1478; Email: brian.bennett@mu.edu
- **Authors**
    - **Wasantha Lankathilaka Karunagala Pathiranage** - *Department of Chemistry, Marquette University, 1414 West Clybourn Street, Milwaukee, Wisconsin 53233, United States*
    - **Natalie Gumataotao** - *Department of Chemistry and Biochemistry, Loyola University, 1068 West Sheridan Road, Chicago, Illinois 60660, United States*

- **Funding**

This work was supported by the National Science Foundation (CHE-1808711 and CHE-1532168 BB & RCH) and the National Institutes of Health (GM 126522 ATF).

- **Notes**

The authors declare no competing financial interest.

References

1 Cheng, Z.; Xia, Y.; Zhou, Z. Recent Advances and Promises in Nitrile Hydratase: From Mechanism to Industrial Applications. *Front. Bioeng. Biotechnol.* **2020**, *8*, 352 DOI: 10.3389/fbioe.2020.00352

2 Kobayashi, M.; Shimizu, S. Cobalt Proteins. *Eur. J. Biochem.* **1999**, *261*, 1– 9, DOI: 10.1046/j.1432-1327.1999.00186.x

3 Harrop, T. C.; Mascharak, P. K. Fe(III) and Co(III) centers with carboxamido nitrogen and modified sulfur coordination: lessons learned from nitrile hydratase. *Acc. Chem. Res.* **2004**, *37*, 253– 260, DOI: 10.1021/ar0301532

4 Jin, H.; Turner, I. M.; Nelson, M. J.; Gurbiel, R. J.; Doan, P. E.; Hoffman, B. M. Coordination Sphere of the Ferric Ion in Nitrile Hydratase. *J. Am. Chem. Soc.* **1993**, *115*, 5290– 5291, DOI: 10.1021/ja00065a048

5 Dey, A.; Chow, M.; Taniguchi, K.; Lugo-Mas, P.; Davin, S.; Maeda, M.; Kovacs, J. A.; Odaka, M.; Hodgson, K. O.; Hedman, B.; Solomon, E. I. Sulfur K-Edge XAS and DFT Calculations on Nitrile Hydratase: Geometric and Electronic Structure of the Non-heme Iron Active Site. *J. Am. Chem. Soc.* **2006**, *128*, 533– 541, DOI: 10.1021/ja0549695

6 Tsujimura, M.; Odaka, M.; Nakayama, H.; Dohmae, N.; Koshino, H.; Asami, T.; Hoshino, M.; Takio, K.; Yoshida, S.; Maeda, M.; Endo, I. A novel inhibitor for Fe-type nitrile hydratase: 2-cyano-2-propyl hydroperoxide. *J. Am. Chem. Soc.* **2003**, *125*, 11532– 11538, DOI: 10.1021/ja035018z

7 Yamanaka, Y.; Kato, Y.; Hashimoto, K.; Iida, K.; Nagasawa, K.; Nakayama, H.; Dohmae, N.; Noguchi, K.; Noguchi, T.; Yohda, M.; Odaka, M. Time-Resolved Crystallography of the Reaction Intermediate of Nitrile Hydratase: Revealing a Role for the Cysteinesulfenic Acid Ligand as a Catalytic Nucleophile. *Angew. Chem., Int. Ed.* **2015**, *54*, 10763– 10767, DOI: 10.1002/anie.201502731

8 Yano, T.; Wasada-Tsutsui, Y.; Arii, H.; Yamaguchi, S.; Funahashi, Y.; Ozawa, T.; Masuda, H. Co(III) Complexes with N2(SO)2-Type Equatorial Planar Ligands Similar to the Active Center of Nitrile Hydratase: Role of the Sulfenate Group in the Enzymatic Reaction. *Inorg. Chem.* **2007**, *46*, 10345– 10353, DOI: 10.1021/ic701107x

9 Kovacs, J. A. Synthetic analogues of cysteinate-ligated non-heme iron and non-corrinoid cobalt enzymes. *Chem. Rev.* **2004**, *104*, 825– 848, DOI: 10.1021/cr020619e

10 Mascharak, P. K. Structural and Functional Models of Nitrile Hydratase. *Coord. Chem. Rev.* **2002**, *225*, 201– 214, DOI: 10.1016/S0010-8545(01)00413-1

11 Rose, M. J.; Betterley, N. M.; Mascharak, P. K. Thiolate S-Oxygenation Controls Nitric Oxide (NO) Photolability of a Synthetic Iron Nitrile Hydratase (Fe-NHase) Model Derived from Mixed Carboxamide/Thiolate Ligand. *J. Am. Chem. Soc.* **2009**, *131*, 8340– 8341, DOI: 10.1021/ja9004656

12 O'Toole, M. G.; Bennett, B.; Mashuta, M. S.; Grapperhaus, C. A. Substrate Binding Preferences and pK_a Determinations of a Nitrile Hydratase Model Complex: Variable Solvent Coordination to [(bmmp-TASN)Fe]OTf. *Inorg. Chem.* **2009**, *48*, 2300– 2308, DOI: 10.1021/ic802180d

13 Gumataotao, N.; Kuhn, M. L.; Hajnas, N.; Holz, R. C. Identification of an active site-bound nitrile hydratase intermediate through single turnover stopped-flow spectroscopy. *J. Biol. Chem.* **2013**, *288*, 15532– 15536, DOI: 10.1074/jbc.M112.398909

14 Stein, N.; Gumataotao, N.; Hajnas, N.; Wu, R.; Lankathilaka, K. P. W.; Bornscheuer, U. T.; Liu, D.; Fiedler, A. T.; Holz, R. C.; Bennett, B. Multiple States of Nitrile Hydratase from *Rhodococcus equi* TG328-2: Structural and Mechanistic Insights from Electron Paramagnetic Resonance and Density Functional Theory Studies. *Biochemistry* **2017**, *56*, 3068– 3077, DOI: 10.1021/acs.biochem.6b00876

15 Martinez, S.; Wu, R.; Sanishvili, R.; Liu, D.; Holz, R. C. The Active Site Sulfenic Acid Ligand in Nitrile Hydratases Can Function as a Nucleophile. *J. Am. Chem. Soc.* **2014**, *136*, 1186– 1189, DOI: 10.1021/ja410462j

16 Prejanò, M.; Marino, T.; Rizzuto, C.; Madrid Madrid, J. C.; Russo, N.; Toscano, M. Reaction Mechanism of Low-Spin Iron(III)- and Cobalt(III)-Containing Nitrile Hydratases: A Quantum Mechanics Investigation. *Inorg. Chem.* **2017**, *56*, 13390– 13400, DOI: 10.1021/acs.inorgchem.7b02121

17 Light, K. M.; Yamanaka, Y.; Odaka, M.; Solomon, E. I. Spectroscopic and computational studies of nitrile hydratase: insights into geometric and electronic structure and the mechanism of amide synthesis. *Chem. Sci.* **2015**, *6*, 6280– 6294, DOI: 10.1039/C5SC02012C

18 Kayanuma, M.; Shoji, M.; Yohda, M.; Odaka, M.; Shigeta, Y. Catalytic Mechanism of Nitrile Hydratase Subsequent to Cyclic Intermediate Formation: A QM/MM study. *J. Phys. Chem. B* **2016**, *120*, 3259– 3266, DOI: 10.1021/acs.jpcb.5b11363

19 Nelp, M. T.; Song, Y.; Wysocki, V. H.; Bandarian, V. A. Protein-derived Oxygen Is the Source of the Amide Oxygen of Nitrile Hydratases. *J. Biol. Chem.* **2016**, *291*, 7822– 7829, DOI: 10.1074/jbc.M115.704791

20 Hopmann, K. H. Full Reaction Mechanism of Nitrile Hydratase: A Cyclic Intermediate and an Unexpected Disulfide Switch. *Inorg. Chem.* **2014**, *53*, 2760– 2762, DOI: 10.1021/ic500091k

21 Mitra, S.; Holz, R. C. Unraveling the Catalytic Mechanism of Nitrile Hydratases. *J. Biol. Chem.* **2007**, *282*, 7397– 7404, DOI: 10.1074/jbc.M604117200

22 Rao, S. N.; Holz, R. C. Analyzing the Catalytic Mechanism of the Fe-Type Nitrile Hydratase from *Comamonas testosteroni* Ni1. *Biochemistry* **2008**, *47*, 12057– 12064, DOI: 10.1021/bi801623t

23 Lankathilaka, K. P. W.; Stein, N.; Holz, R. C.; Bennett, B. Cellular Maturation of an Iron-Type Nitrile Hydratase Interrogated using EPR Spectroscopy. *J. Biol. Inorg. Chem.* **2019**, *24*, 1105– 1113, DOI: 10.1007/s00775-019-01720-y

24 Tsopanakis, A. D.; Tanner, S. J.; Bray, R. C. pH-Jump studies at subzero temperatures on an intermediate in the reaction of xanthine oxidase with xanthine. *Biochem. J.* **1978**, *175*, 879– 885, DOI: 10.1042/bj1750879

25 Bennett, B.; Benson, N.; McEwan, A. G.; Bray, R. C. Multiple states of the molybdenum centre of dimethylsulphoxide reductase from Rhodobacter capsulatus revealed by EPR spectroscopy. *Eur. J. Biochem.* **1994**, *225*, 321– 331, DOI: 10.1111/j.1432-1033.1994.00321.x

26 Bruno, F.; Belusko, M.; Liu, N.; Tay, S. H. Using Solid–Liquid Phase Change Materials (PCMs) in Thermal Energy Storage Systems. In *Advances in Thermal Energy Storage Systems: Methods and Applications*; Cabeza, L. F., Ed.; Woodhead Publishing: Cambridge, U.K., 2014; pp 201– 246.

27 Stoll, S.; Schweiger, A. EasySpin, a comprehensive software package for spectral simulation and analysis in EPR. *J. Magn. Reson.* **2006**, *178*, 42– 55, DOI: 10.1016/j.jmr.2005.08.013

28 Neese, F. *Orca–An Ab Initio, Density Functional and Semiempirical Program Package*, version 3.0; MPI for Chemical Energy Conversion: Mulheim, Germany, 2013.

29 Adamo, C.; Scuseria, G. E.; Barone, V. Accurate excitation energies from time-dependent density functional theory: Assessing the PBE0 model. *J. Chem. Phys.* **1999**, *111*, 2889– 2899, DOI: 10.1063/1.479571

30 Perdew, J. P.; Burke, K.; Ernzerhof, M. Generalized gradient approximation made simple. *Phys. Rev. Lett.* **1996**, *77*, 3865– 3868, DOI: 10.1103/PhysRevLett.77.3865

31 Schäfer, A.; Huber, C.; Ahlrichs, R. Fully Optimized Contracted Gaussian Basis Sets of Triple Zeta Valence Quality for Atoms Li to Kr. *J. Chem. Phys.* **1994**, *100*, 5829– 5835, DOI: 10.1063/1.467146

32 Schäfer, A.; Horn, H.; Ahlrichs, R. Fully Optimized Contracted Gaussian Basis Sets for Atoms Li to Kr. *J. Chem. Phys.* **1992**, *97*, 2571– 2577, DOI: 10.1063/1.463096

33 Stratmann, R. E.; Scuseria, G. E.; Frisch, M. J. An efficient implementation of time-dependent density-functional theory for the calculation of excitation energies of large molecules. *J. Chem. Phys.* **1998**, *109*, 8218– 8224, DOI: 10.1063/1.477483

34 Casida, M. E.; Jamorski, C.; Casida, K. C.; Salahub, D. R. Molecular excitation energies to high-lying bound states from time-dependent density-functional response theory: Characterization and correction of the time-dependent local density approximation ionization threshold. *J. Chem. Phys.* **1998**, *108*, 4439– 4449, DOI: 10.1063/1.475855

35 Bauernschmitt, R.; Ahlrichs, R. Treatment of electronic excitations within the adiabatic approximation of time dependent density functional theory. *Chem. Phys. Lett.* **1996**, *256*, 454– 464, DOI: 10.1016/0009-2614(96)00440-X

36 Hirata, S.; Head-Gordon, M. Time-dependent density functional theory for radicals - An improved description of excited states with substantial double excitation character. *Chem. Phys. Lett.* **1999**, *302*, 375– 382, DOI: 10.1016/S0009-2614(99)00137-2

37 Hirata, S.; Head-Gordon, M. Time-dependent density functional theory within the Tamm-Dancoff approximation. *Chem. Phys. Lett.* **1999**, *314*, 291– 299, DOI: 10.1016/S0009-2614(99)01149-5

38 Taylor, C. P. S. The EPR of Low Spin Heme Complexes. *Biochim. Biophys. Acta, Protein Struct.* **1977**, *491*, 137– 149, DOI: 10.1016/0005-2795(77)90049-6

39 Lugo-Mas, P.; Dey, A.; Xu, L.; Davin, S. D.; Benedict, J.; Kaminsky, W.; Hodgson, K. O.; Hedman, B.; Solomon, E. I.; Kovacs, J. A. How Does Single Oxygen Atom Addition Affect the Properties of an Fe-Nitrile Hydratase Analogue? The Compensatory Role of the Unmodified Thiolate. *J. Am. Chem. Soc.* **2006**, *128*, 11211– 11221, DOI: 10.1021/ja062706k

40 Singh, S. K.; Atanasov, M.; Neese, F. Challenges in Multireference Perturbation Theory for the Calculations of the g-Tensor of First-Row Transition-Metal Complexes. *J. Chem. Theory Comput.* **2018**, *14*, 4662– 4677, DOI: 10.1021/acs.jctc.8b00513

41 Singh, S. K.; Eng, J.; Atanasov, M.; Neese, F. Covalency and chemical bonding in transition metal complexes: An ab initio based ligand field perspective. *Coord. Chem. Rev.* **2017**, *344*, 2– 25, DOI: 10.1016/j.ccr.2017.03.018

42 Weigend, F.; Ahlrichs, R. Balanced basis sets of split valence, triple zeta valence and quadruple zeta valence quality for H to Rn: Design and assessment of accuracy. *Phys. Chem. Chem. Phys.* **2005**, *7*, 3297– 3305, DOI: 10.1039/b508541a

43 Becke, A. D. Density functional thermochemistry. III. The role of exact exchange. *J. Chem. Phys.* **1993**, *98*, 5648– 5652, DOI: 10.1063/1.464913

44 Lee, C. T.; Yang, W. T.; Parr, R. G. Development of the Colle-Salvetti Correlation-energy Formula into a Functional of the Electron Density. *Phys. Rev. B: Condens. Matter Mater. Phys.* **1988**, *37*, 785– 789, DOI: 10.1103/PhysRevB.37.785

45 Angeli, C.; Cimiraglia, R.; Evangelisti, S.; Leininger, T.; Malrieu, J. P. Introduction of n-electron valence states for multireference perturbation theory. *J. Chem. Phys.* **2001**, *114*, 10252– 10264, DOI: 10.1063/1.1361246

46 Kramers, H. A. Brownian motion in a field of force and the diffusion model of chemical reactions. *Physica* **1940**, *7*, 284– 304, DOI: 10.1016/S0031-8914(40)90098-2

47 Jacob, M.; Geeves, M.; Holterman, G.; Schmid, F. X. Diffusional crossing in a two-state protein folding reaction. *Nat. Struct. Biol.* **1999**, *6*, 923– 926, DOI: 10.1038/13289

48 Jacob, M.; Schmid, F. X. Protein folding as a diffusional process. *Biochemistry* **1999**, *38*, 13773– 13779, DOI: 10.1021/bi991503o

49 Demchenko, A. P.; Ruskyn, O. I.; Saburova, E. A. Kinetics of the lactate dehydrogenase reaction in high-viscosity media. *Biochim. Biophys. Acta, Protein Struct. Mol. Enzymol.* **1989**, *998*, 196– 203, DOI: 10.1016/0167-4838(89)90273-2

50 Uribe, S.; Sampedro, S. G. Measuring Solution Viscosity and its Effect on Enzyme Activity. *Biol. Proced. Online* **2003**, *5*, 108– 115, DOI: 10.1251/bpo52

51 Kestin, J.; Khalifa, H. E.; Correia, R. J. Tables of the dynamic and kinematic viscosity of aqueous NaCl solutions in the temperature range 20–150 °C and the pressure range 0.1–35 MPa. *J. Phys. Chem. Ref. Data* **1981**, *10*, 71– 87, DOI: 10.1063/1.555641

52 Yang, A. S.; Brill, A. S. Influence of the Freezing Process upon Fluoride Binding to Hemeproteins. *Biophys. J.* **1991**, *59*, 1050– 1063, DOI: 10.1016/S0006-3495(91)82320-7

53 Toner, J. D.; Catling, D. C.; Light, B. The formation of supercooled brines, viscous liquids, and low-temperature perchlorate glasses in aqueous solutions relevant to Mars. *Icarus* **2014**, *233*, 36– 47, DOI: 10.1016/j.icarus.2014.01.018

54 Incorpera, F. P.; DeWitt, D. P.; Bergman, T.; Lavine, A. S. *Fundamentals of Heat and Mass Transfer*; John Wiley & Sons: New York, 2007.

55 Holten, V.; Bertrand, C. E.; Anisimov, M. A.; Sengers, J. V. Thermodynamics of Supercooled Water. *J. Chem. Phys.* **2012**, *136*, 094507 DOI: 10.1063/1.3690497

56 Griffith, J. S. Theory of electron resonance in ferrihemoglobin azide. *Nature* **1957**, *180*, 30– 31, DOI: 10.1038/180030a0

57 Fischer, A. A.; Miller, J. R.; Jodts, R. J.; Ekanayake, D. M.; Lindeman, S. V.; Brunold, T. C.; Fiedler, A. T. Spectroscopic and Computational Comparisons of Thiolate-Ligated Ferric Nonheme Complexes to Cysteine Dioxygenase: Second-Sphere Effects on Substrate (Analogue) Positioning. *Inorg. Chem.* **2019**, *58*, 16487– 16499, DOI: 10.1021/acs.inorgchem.9b02432